Materials Advances

ROYAL SOCIETY OF CHEMISTRY

PAPER

View Article Online
View Journal | View Issue

Cite this: *Mater. Adv.*, 2025, **6**, 7409

A hybrid polyaniline/dolomite–palygorskite framework for environmental remediation: experimental design and molecular-level adsorption interpretation

Samira El Omari,*[ab] Abdelaziz Imgharn,*[a] Youness Abdellaoui,[cd] Oscar May Tzuc,[e] Abdallah Albourine,[af] Lahcen Bazzi,[f] Mohamed Laabd*[a] and Karim Benhabib[b]

Textile and dyestuff manufacturing industries are recognized as the largest source of water contamination. This study explores the effectiveness of the polyaniline@dolomite–palygorskite clay (PANi@DPC) hybrid composite for removing orange G (OG) dye from polluted water through adsorption. The PANi@DPC composite was analyzed by scanning electron microscopy (SEM) coupled with energy dispersive spectroscopy (EDS), Fourier transform infrared (FTIR) spectroscopy and X-ray diffraction (XRD). The main findings prove the successful incorporation of PANi on the palygorskite surface. The PANi@DPC composite exhibited an open morphology richly decorated with nitrogen/oxygen-containing functionalities (*e.g.*, –NH, ═NH and –OH), which boosts the diffusion and adsorption of OG dye. The OG dye adsorption experiments were conducted to assess the effect of the operational parameters. The PANi@DPC composite exhibited an impressive removal performance (>97.75%) for OG dye over a broad pH range of 2.6–8.4. Kinetics and isotherm data were adequately simulated by the pseudo-second order (R^2 = 0.997) and Freundlich (R^2 = 0.991) models. The PANi@DPC composite was effortlessly regenerated and efficiently reused for OG removal. FTIR analysis suggested that the adsorption mechanism is predominantly mediated by H-bonds and π–π stacking. Applying a response surface methodology, the highest OG removal performance of 99.54% was achieved under the optimal conditions of pH 6.0, 1.0 g L^{-1} PANi@DPC dose, 20 mg L^{-1} initial OG concentration, 120 min contact time and 25 °C. Advanced statistical physics simulation revealed that the OG adsorption follows multi-anchorage and multi-molecular binding mechanisms. Overall, the PANi@DPC hybrid composite can serve as a prospective binder material for cleaning up the OG dye-containing wastewater.

Received 20th June 2025,
Accepted 26th August 2025

DOI: 10.1039/d5ma00660k

rsc.li/materials-advances

1. Introduction

Nowadays, the extensive application of synthetic dyes across various manufacturing fields has led to the production of enormous quantities of dye-contaminated effluents.[1] The discharge of these effluents poses a potential danger to biodiversity and human health.[2] Azo dyes are a widespread class of commercialized colorants, and they represent approximately 60% of the synthetic dyes utilized in industrial processes.[3] Azo dyes are aromatic organic molecules with azo groups (–N═N–), making them resistant to biodegradation with potential harmful outcomes.[4] Moreover, the metabolic byproducts of azo dyes (*e.g.*, 1,4-phenylenediamine, *o*-tolidine and benzene sulfonic acids) are widely recognized as carcinogenic and mutagenic compounds.[5] Consequently, they can induce potentially detrimental effects such as cytotoxicity and genotoxicity on cells.[6] The presence of dyes as coloring substances in aquatic

[a] *Laboratory of Materials and Environment, Faculty of Sciences, Ibnou Zohr University, Agadir, Morocco. E-mail: samiraelomari.00@gmail.com, abdelaziz.imgharn@edu.uiz.ac.ma, m.laabd@uiz.ac.ma*
[b] *Eco-Process, Optimization and Decision Support. Jules Verne University of Picardie (EPROAD, UR), France*
[c] *Cinvestav Saltillo. Sustainability of Natural Resources and Energy, Av. Industria Metalúrgica 1062, Parque Industrial Ramos Arizpe, Ramos Arizpe, Coahuila C.P. 25900, Mexico*
[d] *CONAHCyT-Cinvestav Saltillo. Sustainability of Natural Resources and Energy, Av. Industria Metalúrgica 1062, Parque Industrial Ramos Arizpe, Ramos Arizpe, Coahuila C.P. 25900, Mexico*
[e] *Faculty of Engineering, Autonomous University of Campeche, Campus V, Av Humberto Lanz, Col. Ex Hacienda Kalá, C.P. 24085, San Francisco de Campeche, Campeche, Mexico*
[f] *Laboratory of Industrial Engineering, Energy and Environment (LI3E), SupMTI Rabat, Rabat 10000, Morocco*

ecosystems reduces sunlight penetration.[7] This significantly disrupts crucial processes such as photosynthesis, ultimately leading to a notable decrease in water oxygenation capacity (dissolved oxygen level).[7] Thus, the decontamination of dyed effluents has emerged as an urgent worldwide issue for ecologists aiming to preserve ecosystems.

Numerous wastewater treatment technologies such as photocatalytic degradation,[8,9] adsorption,[10] coagulation/flocculation[11] and membrane filtration[12] have been employed for treating contaminated effluents. The photocatalysis represents a sustainable strategy for eliminating organic pollutants.[13,14] In photocatalysis, a semiconductor absorbs light energy to generate reactive oxygen species that break down toxic organic contaminants into harmless molecules (*e.g.*, H_2O, CO_2 and inorganic ions).[15–17] Despite its advantages, the photocatalytic degradation technique is hindered by some shortcomings such as high energy demand, high operational costs, long processing times and low efficiency in treating concentrated textile dyeing effluent due to limited light penetration.[18,19] Adsorption has emerged as one of the most prevalent and reliable techniques.[20,21] This technique offers distinct advantages such as straightforward design, cost-effectiveness, and suitability for large-scale implementation.[20] From an operational standpoint, the development of efficient and easily recyclable adsorbents is highly desirable.

In the past decade, natural clays (hydrous aluminosilicate minerals) have been extensively investigated as adsorbents for wastewater treatment owing to their remarkable characteristics (*e.g.*, low-cost, high surface area, superior mechanical strength and stability, safety, ion exchange capacity, surface charge and hydrophilicity).[22] Nonetheless, the clay minerals tend to form stable colloidal suspensions in water due to their fine grain size, which restricts their separation, reuse and effectiveness in fixed-bed systems (low permeability).[23] Furthermore, the natural clays exhibited a very low uptake performance for anionic and neutral contaminants owing to their negative surfaces.[24]

Polyaniline (PANi), a conjugated polymer, has garnered considerable interest recently due to its distinctive features, including good environmental stability, non-toxicity, low monomer prices, reversible redox chemistry, antibacterial activity, and facile synthesis.[25] The imine/amine functional moieties and aromatic hydrocarbon structures of PANi can act as receptor sites for water contaminants.[26] Furthermore, the reversible acid–base doping/de-doping character of PANi contributes significantly to the regeneration of PANi-based adsorbents.[27] Nevertheless, the pure PANi faces some inherent demerits like poor dispersion ability and vulnerability to aggregation in irregular form in water, which may reduce the active surface area of PANi in aqueous media.[21] Consequently, current research is increasingly focused on hybridizing PANi with inorganic materials for the effective removal of water contaminants under milder pH conditions.[21]

Combining PANi with clay minerals yields a synergistic effect, where PANi enhances surface activity and adsorption affinity, while the clay minerals improve structural stability, dispersion, and surface area. This integration not only mitigates the aggregation issues of the pure PANi polymer but also enables efficient dye removal under near-neutral pH conditions. Thus, it expands the practical applicability of the resulting composites in wastewater treatment. In the current study, PANi was synthesized *via* oxidative polymerization of the aniline using sodium persulfate as a free radical initiator in the presence of dolomite–palygorskite clay (DPC) mineral particles. The resulting PANi@DPC hybrid composite was thoroughly characterized using scanning electron microscopy (SEM) coupled with energy dispersive spectroscopy (EDS), Fourier transform infrared (FTIR) spectroscopy, and X-ray diffraction (XRD), and then utilized as an adsorbent to remove the orange G (OG) dye, a typical azo dye, from the aqueous phase. The effects of influencing parameters on OG dye decolorization performance were systematically assessed. The adsorption kinetics and isotherms were examined. To elucidate the OG binding mechanism at the molecular scale, the adsorption equilibrium data were deeply analyzed using advanced statistical physics formalism. Furthermore, the mutual interactive effects of the influencing factors on the OG dye adsorption process were statistically evaluated *via* response surface modeling combined with Box–Behnken design (RSM-BBD). Finally, the reusability of the PANi@DPC hybrid composite was investigated.

2. Materials and methods

2.1. Chemicals

Prior to polymerization, the aniline monomer ($C_6H_5NH_2$, $\geq$99.5%) was freshly distilled. Sodium persulfate ($Na_2S_2O_8$, $\geq$98%), ethanol, hydrochloric acid (HCl, 37%), sodium hydroxide (NaOH, $\geq$97.0%), potassium nitrate (KNO_3, $\geq$99.0%), sodium nitrate ($NaNO_3$, $\geq$99.0%), sodium sulfate ($NaSO_4$, $\geq$99.0%), sodium bicarbonate ($NaHCO_3$, $\geq$99.7%) and OG dye ($C_{16}H_{10}N_2Na_2O_7S_2$, 80%) were of reagent grade and were supplied by Sigma-Aldrich. The natural clay was collected from the Marrakech region (Morocco). After crushing, the collected clay was sieved to obtain an average particle size of less than 50 μm.

2.2. PANi@DPC hybrid composite preparation

The PANi@DPC hybrid composite was prepared by means of the oxidative polymerization method of aniline monomer in the presence of the DPC particles. Briefly, 1 mL of distilled aniline was poured into 50 mL of HCl (1 M) containing 1 g of the DPC. The mixture was then stirred for 60 min to ensure a uniform distribution of the clay particles. On the other hand, 5.23 g of $Na_2S_2O_8$ were dissolved in 50 mL of HCl (1 M). The next step was to introduce the oxidizing solution ($Na_2S_2O_8$) into the monomer solution under stirring for 8 h. In addition to the filtration process, the resultant dark green precipitate was cleaned with distilled water, followed by ethanol and dried at 60 °C for 12 h. A schematic illustration of the synthesis process is depicted in Fig. 1.

2.3. Instrumentations

The XRD technique was used to analyze the structural features of DPC and the PANi@DPC composite using an EMPYREAN PANALYTICAL instrument (PANalytical Co., Netherlands). The

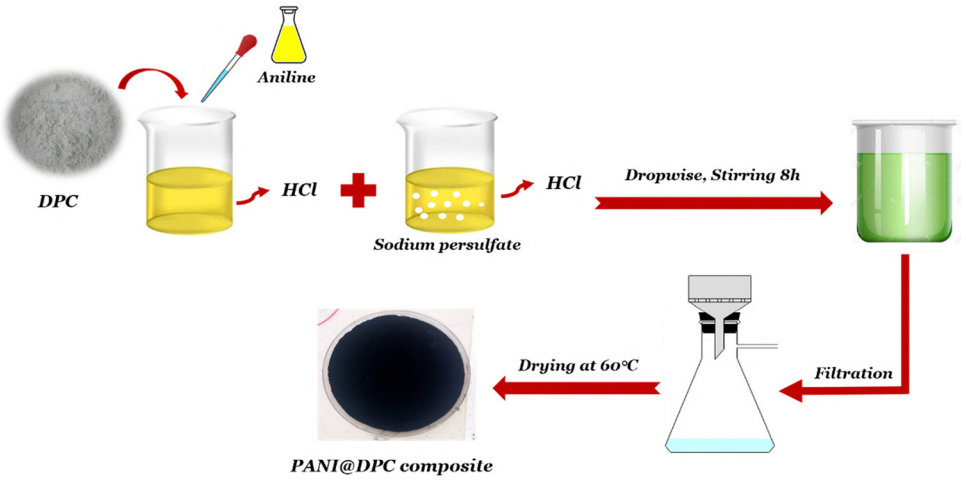

Fig. 1 Schematic diagram of the fabrication process of the PANi@DPC hybrid composite.

XRD diffractograms were recorded in the 2θ range of 5–60° using a beam of Cu radiation at 40 kV and 25 mA. To visualize the surface morphologies of DPC and the PANi@DPC composite, the SEM coupled with EDS analysis was carried out using a JEOL JSM-IT100 microscope at a 15 kV beam voltage. FTIR spectral analysis of samples was accomplished employing a Nicolet 5700 FTIR spectrophotometer (Thermo Nicolet Co., USA) with KBr pellets covering a spectral range of 400–4000 cm^{-1}.

The point of zero charge (PZC) value of PANi@DPC surface was acquired through the salt addition method.[28] A series of mixtures was obtained by dispersing 30 mg of PANi@DPC composite in 50 mL of 0.03 M KNO_3. The initial pH (pH_i) values of the resulting mixtures were adjusted from 2.0 to 9.4 by NaOH or HCl solutions and kept for 48 h under continuous stirring to reach equilibrium. The equilibrium pH (pH_f) values were measured and the PZC value of PANi@DPC was determined at pH_i where $pH_f - pH_i = 0$.

2.4. Adsorption and regeneration experiments

The effectiveness of the PANi@DPC composite for removing OG dye was assessed under different operating conditions. The effect of sorbent dose was examined by adding different PANi@DPC amounts ranging from 0.125 to 1 g L^{-1} into 20 mL of 25 mg L^{-1} OG solution. To assess the influence of solution pH on the OG dye removal performance, the solution pH was varied from 2.6 to 9.8 while keeping the other parameters unchanged. Similarly, the adsorption equilibrium was investigated over an OG initial concentration range between 20 and 300 mg L^{-1}. The OG uptake capacity was studied by varying the contact time from 5 to 150 min. The effect of interfering ions (*e.g.*, NO_3^-, SO_4^{2-} and HCO_3^-) on the OG removal performance by PANi@DPC composite was also investigated. After each adsorption assay, a microfiltration step is required to separate the PANi@DPC from the solution using a 0.45 μm filter. After adsorption tests, OG dye concentration was quantified using a 2300 UV-visible spectrophotometer at 476 nm.[29]

The removal efficiency R (%) and adsorbed amount Q_e (mg g^{-1}) are computed using the equations given below.[30]

$$R\ (\%) = \frac{(C_i - C_e) \times 100}{C_e} \quad (1)$$

$$Q_e = \frac{(C_i - C_e) \times V}{m} \quad (2)$$

where C_i and C_e represent the initial and residual OG concentrations (mg L^{-1}), while V (L) denotes the volume of OG solution. The amount of PANi@DPC composite is denoted as m (g).

After adsorption tests, the regeneration process of spent PANi@DPC adsorbent is a critical step in reducing operational costs and environmental impact. The adsorbent reusability was assessed by introducing 0.15 g of the PANi@DPC composite into 400 mL of 25 mg L^{-1} OG solution for 2 h. Then, the desorption process was done using 0.5 M NaOH solution as eluent for 2 h at ambient temperature. The recovered composite was rinsed with distilled water and then reactivated through a doping step using a 0.5 M HCl solution. The same procedure was repeated for the next regeneration cycle up to five times.

2.5. RSM-BBD modeling

RSM and artificial neural networks (ANN) are commonly employed in adsorption modeling and optimization, yet each offers distinct advantages. RSM facilitates the development of interpretable polynomial models, generates visualizable three-dimensional (3D) response surfaces, and enables statistical evaluation of variable interactions using relatively few experiments.[31] In contrast, ANN offers greater flexibility in capturing the non-linear relationships between input and output variables without requiring a predefined functional form.[32] Overall, while ANN often outperforms RSM in predictive accuracy (especially under strong nonlinearity), RSM remains a valuable tool for experimental planning, identifying optimal

operational conditions, and providing direct insight into variable effects.[33,34]

In the present work, the RSM-based BBD method executed in the Design-Expert 13.0 program was used to assess the effects of PANi@DPC dosage (X_A), OG dye concentration (X_B) and pH (X_C) on the OG removal efficiency (Y). Each process factor was set to three levels: −1 (minimal), 0 (intermediate) and +1 (maximal). The experimental design matrix consisted of 17 combinations as shown in Table S1. Actual data were fitted to a quadratic polynomial model to establish the relationship between OG dye removal efficiency (Y) and adsorption process factors (X_A, X_B and X_C). The mathematical equation of this model was defined as follows:[35]

$$Y = a_0 + a_1X_A + a_2X_B + a_3X_C + a_{12}X_{A/B} + a_{13}X_{A/C} + a_{23}X_{B/C} + a_{11}X_A{}^2 + a_{22}X_B{}^2 + a_{33}X_C{}^2 \quad (3)$$

where Y denotes the predicted removal efficiency (%). a_0 is constant. $a_{i(=1,2,3)}$ represents the linear coefficients. a_{ij} denotes the coefficients of interactive effects. a_{ii} represents the squared coefficients.

2.6. Advanced statistical physics modeling

Recently, advanced statistical physics has become a non-traditional and impressive methodology to predict the adsorption mechanism at the molecular scale.[36] The energetic and steric properties of the OG binding on the PANi@DPC surface were investigated through various generic scenarios using five mathematical models deriving from advanced statistical physics (Table 1). The 1st model (M1) presumes that the adsorption process happened as a single layer coverage, but a variable number of adsorbates can be bound to each active site. The 2nd model (M2) represents the monolayer adsorption of target dye molecules over two energetically different binding sites. The 3rd model (M3) suggests the adsorption *via* double layers of adsorbate molecules on similar binding sites (homogeneous surface). The 4th model (M4) predicts the double-layer coverage of OG molecules onto the PANi@DPC surface containing two different active sites. The last model (M5) supposes a multiple-layer formation of OG molecules onto the PANi@DPC surface. The appropriateness of these models to predict the OG dye adsorption process was assessed using the determination coefficient (R^2) and root mean squared error (RMSE).

3. Results and discussion

3.1. Characterization

The DPC and the PANi@DPC composite were analyzed using the XRD technique (Fig. 2). The XRD pattern of DPC revealed two diffraction peaks at 8.5° and 19.8° corresponding to the (1 1 0) and (0 4 0) planes, respectively.[37] These crystalline planes are consistent with those of the palygorskite phase, with the chemical formula $Si_{16}Mg_8O_{60}$ (JCPDS: 96-900-5566). In addition, the 2θ peaks observed at 20.85° and 26.65° associated with (1 0 0) and (1 0 1) planes are attributed to the quartz phase with the chemical formula SiO_2 (JCPDS: 96-900-9667).[38] Similarly, the dolomite phase is characterized by three peaks at 2θ values of 30.94° (0 1 4), 41.12° (1 1 3) and 44.92° (0 2 2), which corresponds to JCPDS: 96-900-4933.[39] According to the XRD findings, it can be inferred that natural clay is mainly composed of dolomite and palygorskite phases with a small amount of quartz.[40] Compared to the pristine DPC, the XRD patterns of PANi@DPC composite displayed the occurrence of

Table 1 Formulas of the statistical physics models used for assessing the OG adsorption onto the PANi@DPC surface[36]

Models	Equations
Single layer with a single type of binding site model (M1)	$Q_{ads} = \frac{nN_M}{1+\left(\frac{C_{hs}}{C_e}\right)^n}$
Monolayer with two types of binding sites model (M2)	$Q_{ads} = \frac{n_1N_{1M}}{1+(C_{hs1}/C_e)^{n_1}} + \frac{n_2N_{2M}}{1+(C_{hs2}/C_e)^{n_2}}$
Double layer with a single type of binding site model (M3)	$Q_{ads} = nN_M\frac{\left(\frac{C_e}{C_{hs}}\right)^n+2\left(\frac{C_e}{C_{hs}}\right)^{2n}}{1+\left(\frac{C_e}{C_{hs}}\right)^n+\left(\frac{C_e}{C_{hs}}\right)^{2n}}$
Double layer with two types of binding site model (M4)	$Q_{ads} = nN_M\frac{\left(\frac{C_e}{C_{hs1}}\right)^n+2\left(\frac{C_e}{C_{hs2}}\right)^{2n}}{1+\left(\frac{C_e}{C_{hs1}}\right)^n+\left(\frac{C_e}{C_{hs2}}\right)^{2n}}$
Multilayer model (M5)	$Q_{ads} = nN_M\frac{\left(\frac{C_e}{C_{hs1}}\right)^n\left(1-(N_\ell+1)\left[\frac{C_e}{C_{hs2}}\right]^{nN_\ell}+N_\ell\left[\frac{C_e}{C_{hs2}}\right]^{n(N_\ell+1)}\right)}{\left(1-\left[\frac{C_e}{C_{hs2}}\right]^n\right)\left(1-\left[\frac{C_e}{C_{hs2}}\right]^n+\left[\frac{C_e}{C_{hs1}}\right]^n-\left[\frac{C_e}{C_{hs1}}\right]^n\left[\frac{C_e}{C_{hs2}}\right]^{nN_\ell}\right)}$

where n (dimensionless) signifies the number of captured OG dye molecules per adsorptive site, N_M (mg g^{-1}) is the binding site density. C_{hs} (mg L^{-1}) is the half-saturation concentration of the formed monolayer. C_{sh1} and C_{sh2} (mg L^{-1}) stand for the half-saturation concentrations for the initial and subsequent adsorbed layers. n_1 and n_2 denote the number of OG dye molecules per binding site for the initial and the second type of adsorption sites. (N_ℓ + 1) signifies the number of adsorbed layers.

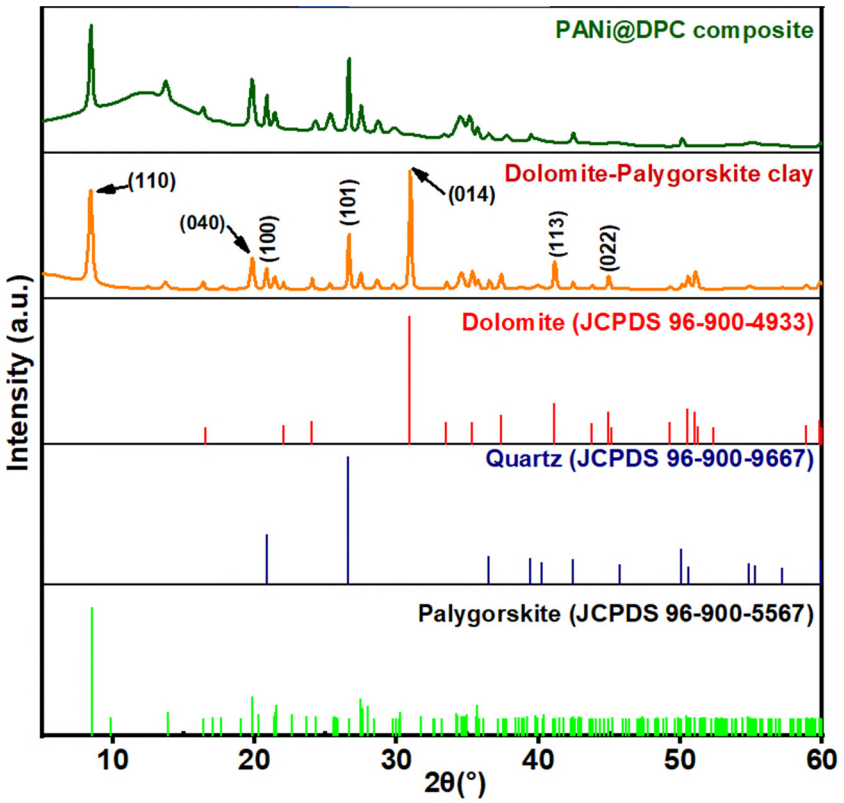

Fig. 2 XRD patterns of DPC and the PANi@DPC composite.

palygorskite and quartz phases, while the dolomite phase was not detected. This result may be ascribed to the complete dissolution of the dolomite phase in HCl solution during the preparation of the PANi@DPC composite according to the following reaction:[41]

$$CaMg(CO_3)_2 + 4H^+ \rightarrow Ca^{2+} + Mg^{2+} + 2CO_2 + 2H_2O \quad (4)$$

Moreover, a very extended broad peak is observed in the XRD diffractogram of the PANi@DPC composite, characterizing the typically amorphous nature of PANi.[42] The diffraction peak characteristics of the palygorskite phase are slightly shifted because of the interactions with the PANi polymer in the resulting PANi@DPC hybrid composite.

SEM-EDS analysis was employed to screen the morphological characteristics and composition of the synthesized composite. Fig. 3 illustrates the morphology analysis of DPC before and after the polymerization of the aniline monomer. As shown in Fig. 3(a), palygorskite takes the form of elongated particles with different sizes and lengths with random orientations, while dolomite is typically represented as rhombohedral-shaped particles with cavities. Furthermore, the figure clearly shows the inter-textual structure between the two minerals, where the palygorskite crystals and dolomite particles superimpose and interlace harmoniously, implying the growth of palygorskite in dolomite cavities.[43] On the other hand, Fig. 3(b) shows that the DPC surface was completely covered with the PANi polymer, confirming that the PANi@DPC hybrid composite was successfully formed.

EDS analysis reveals the elemental chemical composition of the DPC and the PANi@DPC composite (Fig. 3(c) and (d)). The EDS spectrum of DPC clay (Fig. 3(c)) shows several peaks corresponding to C, O, Mg, Al, Si, K, Ca and Fe as the substantial elements on the clay surface. Except for the peak assigned to the Ca element, all other peaks are observed in the EDS spectrum of the PANi@DPC composite (Fig. 3(d)). It is further worth mentioning that there is a significant increase in the mass percentage of carbon as well as the appearance of peaks characteristic of the nitrogen (N), sulfur (S) and chlorine (Cl) elements. This result affirms the successful deposition of PANi on the DPC surface. The disappearance of the EDS peak attributed to the Ca element matches well with the XRD analysis, demonstrating the complete dissolution of the dolomite phase during the preparation of the PANi@DPC composite. Fig. 3(e) illustrates the element mapping images of PANi@DPC hybrid composite. As a result, the elements associated with the PANi polymer (C, N, S and Cl) are distributed almost homogeneously over the surface of the PANi@DPC composite, whereas the other elements are mainly concentrated on the surface of palygorskite particles. The element mapping micrographs further confirm the successful synthesis of the PANi@DPC hybrid composite.

The FTIR spectra of DPC and the PANi@DPC composite are depicted in Fig. 4. In the spectrum of DPC, the absorption bands detected at 3614 and 3556 cm^{-1} correspond to the stretching vibrations of hydroxyl groups.[44] The absorbance

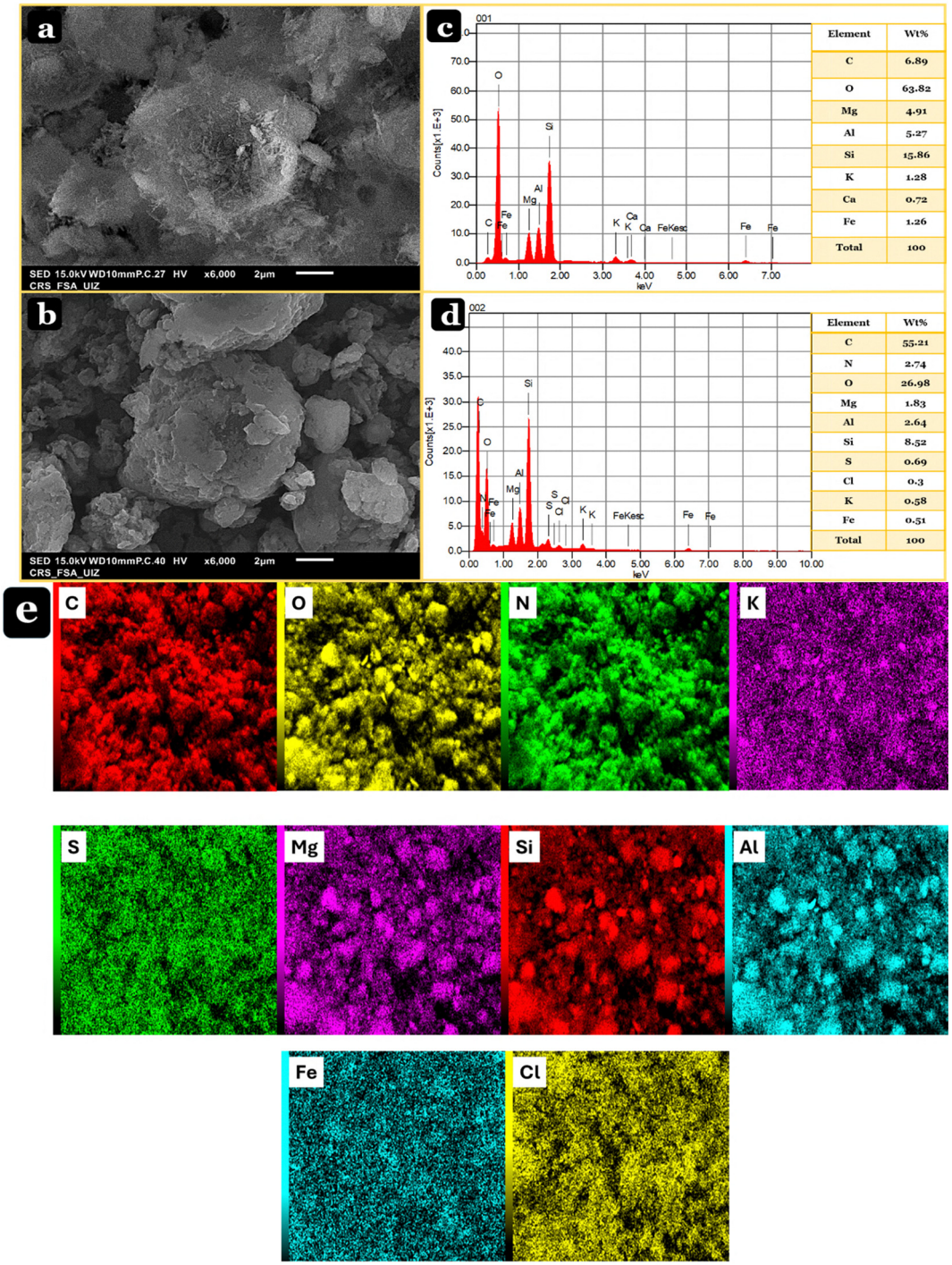

Fig. 3 SEM micrographs of (a) DPC and (b) the PANi@DPC composite and their respective EDS spectra (c) and (d) and (e) EDS elemental maps of the PANi@DPC composite.

bands at 3376, 3266 and 1654 cm^{-1} characterized the zeolitic and coordinate water molecules in the palygorskite phase.[45] The characteristic peak appearing around 1190 cm^{-1} can be assigned to the asymmetric elongation of Si–O–Si.[45] The distinctive bands around 979 and 875 cm^{-1} may be ascribed to Si–O and Si–O–H stretching vibrations, respectively.[45] The vibration peak located at 678 cm^{-1} is indicative of the quartz phase.[46] Furthermore, the FTIR spectrum of DPC confirms the occurrence of the characteristic absorption band of the dolomite phase at 729 cm^{-1}. This peak is caused by bending vibrations of CO_3^{2-} anions.[47] The Mg–O vibration is observed at 542 cm^{-1}.[48] Compared to DPC, new peaks appear in the FTIR spectrum of the PANi@DPC composite at 1598 and 1446 cm^{-1} due to the C=N and C=C stretching vibration of the quinonid and benzenoid structures.[42] The vibration peak appearing at 1301 cm^{-1} is representative of C–N stretching vibrations of

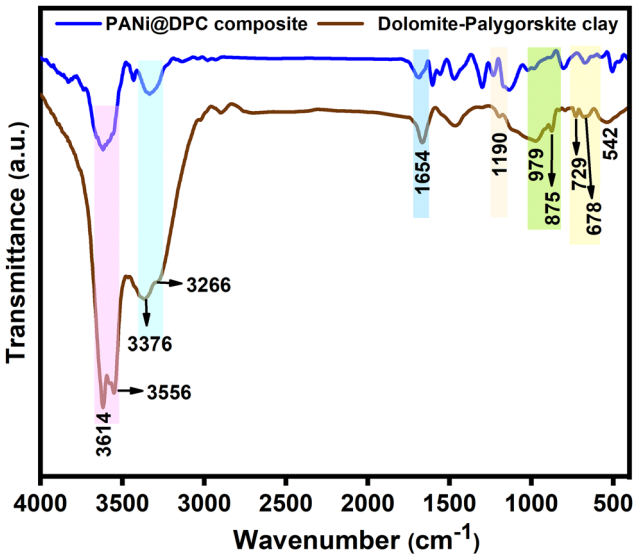

Fig. 4 FTIR spectra of DPC and the PANi@DPC composite.

aromatic amines.[49] The peak at 1138 cm^{-1} reflects the vibrations of protonated amine moieties between quinonid and benzenoid rings.[49] Besides, the spectral peak at 3439 cm^{-1} may be assigned to N–H stretching vibrations. Notably, the –OH peak intensity of the PANi@DPC composite is weaker than that of DPC. This phenomenon could be caused by the cleavage of the intermolecular hydrogen bonds of palygorskite, resulting in the accessibility of more –OH moieties in the palygorskite surface. This facilitates the uniform deposition of PANi on the palygorskite particles *via* interactions between –NH/=NH (amine and imine) and –OH groups.[50] Therefore, the FTIR analysis affirms the successful polymerization of PANi (emeraldine salt form) on the DPC surface. The vibrational peak related to the dolomite phase disappeared after the polymerization reaction due to dolomite dissolution, which agrees with XRD and EDS analyses.

3.2. Adsorption study

3.2.1. Effects of the PANi@DPC dosage and solution pH. The adsorbent dose has been regarded as one of the critical parameters controlling the overall cost of the wastewater remediation process.[51] The OG removal performance was examined by varying PANi@DPC dose from 0.125 to 1 g L^{-1}, as displayed in Fig. 5(a). The outcomes reveal a significant increment in the OG removal percentage as the PANi@DPC dose rises from 0.125 to 0.375 g L^{-1}. This observation is mainly attributed to the enhancement of free receptor sites for OG adsorption. However, it is noted that the adsorption percentage remained stable when the PANi@DPC dosage exceeded 0.375 g L^{-1}. This adsorption tendency might be explained by the agglomeration of PANi@DPC particles (overlapping of active sites).[49] Moreover, the adsorption capacity tends to be reduced as the dose of adsorbent increases, which is probably attributed to the cleavage in adsorbed OG dye molecules by a unit mass of the PANi@DPC adsorbent and the partial utilization of active sites.[49] Considering the OG removal efficiency as well as the economic aspect, 0.375 g L^{-1} was selected as the best PANi@DPC dose.

pH is a key operational factor influencing the interactions at the adsorbent–adsorbate interface. The experimental outcomes illustrating the influence of initial pH on the OG decolorization performance are depicted in Fig. 5(b). The surface ionization state of the adsorbent depends strongly on the solution pH. For this reason, the PANi@DPC surface charge was investigated (Fig. 5(c)). Resultingly, the PZC value was found to be 2.0, indicating that the PANi@DPC surface has a positive charge at pH values less than 2.0, while it exhibits a negative charge at pH values beyond 2. From the experimental data, OG decolorization efficiency is almost stable in the pH range of 2.6–8.4. This adsorption behavior suggests that the OG binding mechanism onto the PANi@DPC composite is mainly governed by non-electrostatic interactions (*e.g.*, π–π interactions and hydrogen bonds).[52] At pH values above 8.4, the OG adsorption performance reduced from 97.75 to 86.12%. This might be due to the competitive adsorption phenomenon between the anionic OG dye and excess hydroxyl ions for the limited binding sites on the PANi@DPC surface. Overall, the as-developed PANi@DPC adsorbent is suitable for OG dye removal across a broad pH range of 2.6–8.4. All the other OG adsorption assays were accomplished at the natural pH (~6.17) of the OG dye solution without any adjustment.

3.2.2. Kinetics and isotherms. The kinetic study is of prime importance for exploring the OG adsorption behavior towards the PANi@DPC surface sites. The effect of adsorption time on the OG adsorption performance of the PANi@DPC composite was assessed. The experimental findings are illustrated in Fig. 6(a). It is clearly seen that the OG adsorption capacity increased as the contact time extended. Also, it is worth mentioning that the OG uptake increased rapidly during the first 15 min, and then dropped down progressively until it reached an equilibrium state after 60 min. In addition, Fig. S1(a) illustrates the effect of contact time on the OG dye removal percentage. The OG dye removal efficiency exhibited a similar trend to that of the adsorption capacity. The observed adsorption trend can result from the excessive free bending sites at the initial adsorption stage. Besides, at this stage, the OG dye concentration was higher, which favors the diffusion of OG molecules driven by the concentration gradient.[53] Nonetheless, with the prolongation of contact time, the vacant binding sites decreased. The repulsion forces between adsorbed OG dye molecules and those in the solution represent another factor that declines the adsorption rate.[54]

The experimental outcomes were examined using three kinetic models, including pseudo-first order (PFO), pseudo-second order (PSO) and intraparticle diffusion (IPD) models. Table 2 summarizes the equations,[35] correlation coefficients (R^2) and fitting parameters of the aforementioned kinetic models. According to R^2 values, the PSO model (R^2 = 0.997) best fitted the experimental data compared to the PFO one. In addition, the ability of the PSO model to predict OG adsorption was confirmed by the good agreement between the theoretical uptake capacity ($Q_{e.cal}$ = 66.71 mg g^{-1}) and that obtained experimentally ($Q_{e.exp}$ = 65.65 mg g^{-1}).

From Fig. 6(b), the results of the IPD model indicate that OG dye adsorption onto the PANi@DPC composite takes place in

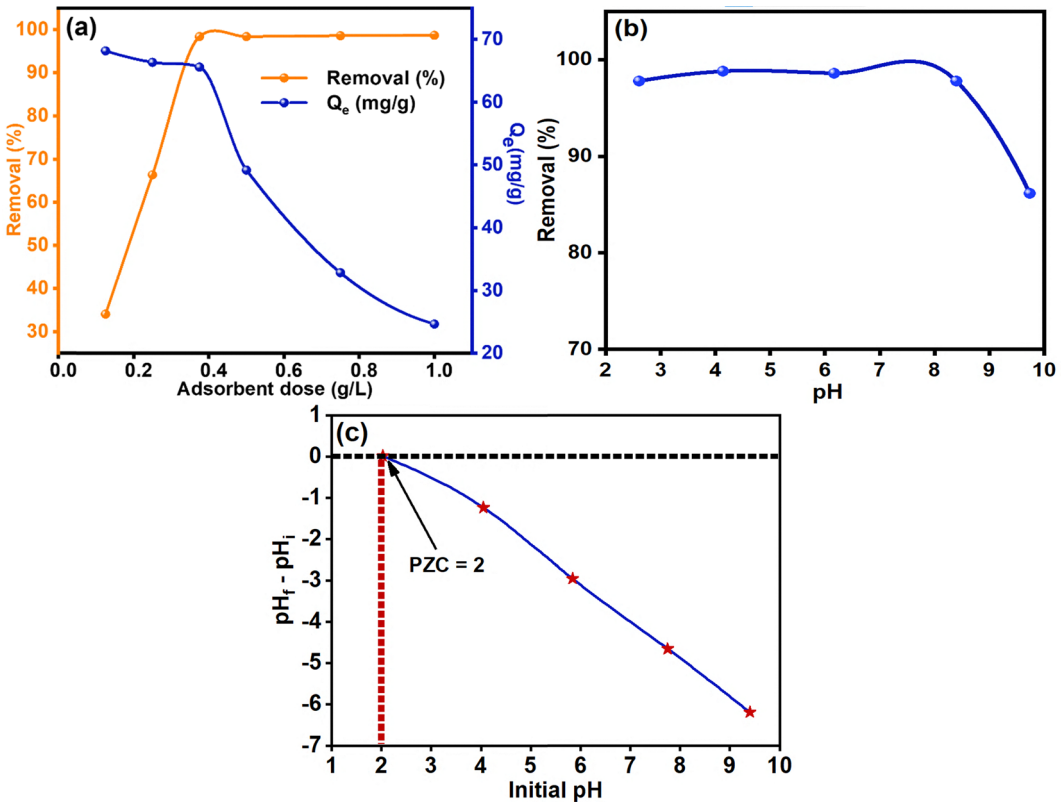

Fig. 5 (a) Effect of the PANi@DPC dosage on the OG decolorization performance (conditions: pH = 6.17; adsorption time = 2 h; OG concentration = 25 mg L^{-1}; T = 25 °C), (b) evolution of OG dye removal performance as a function of pH (conditions: PANi@DPC dose = 0.375 g L^{-1}; contact time = 2 h; OG concentration = 25 mg L^{-1}; T = 25 °C) and (c) PZC determination of the PANi@DPC composite.

two stages, represented by two linear portions. The first one involves fast adsorption onto the outer surface of the PANi@DPC composite. The second step corresponds to the penetration of OG molecules into the adsorbent pores, followed by progressive adsorption on the internal adsorption sites. As reported in Table 2, the value of the IPD constant associated with the first stage (k_{IPD1} = 4.469 mg g^{-1} $min^{-1/2}$) is higher than that of the second stage (k_{IPD2} = 0.215 mg g^{-1} $min^{-1/2}$). These results indicate that the OG removal rate drastically diminished when progressing from the initial to the last stage. Conversely, the boundary layer thickness (C) increased during OG adsorption on the PANi@DPC composite, showing that film diffusion plays a prominent role in the mass transport process.

The effect of the initial OG concentration on the adsorption capacity (Fig. 6(c)) and removal percentage (Fig. S1(b)) was assessed in the range of 20–300 mg L^{-1}. It is noteworthy that the increment in OG concentration led to an increase in the uptake capacity. This adsorption behavior is mainly due to the increment in the concentration gradient, which enhances mass transfer at the solution–adsorbent interface. Therefore, the diffusion of CV dye molecules is more effective at higher OG dye concentrations.[55] As depicted in Fig. S1(b), the OG adsorption percentage was inversely dependent on the OG dye concentration. The gradual decrease in OG removal percentage with increasing its initial concentration may be attributed to the saturation of the binding sites of the PANi@DPC composite. A similar observation was reported by Deb *et al.* for the adsorption of eriochrome Black-T dye on the iron oxide–PANi–PNC nanocomposite.[56]

The analysis of adsorption isotherms is useful to illuminate the distribution of OG molecules at the solution–PANi@DPC composite interface. Fig. 6(c) illustrates the non-linear fitting of Langmuir, Freundlich and Temkin equations to the actual results. The adsorption isotherm equations[35] and their corresponding fitting parameters are listed in Table 2. As a result, the correlation coefficient associated with the Freundlich isotherm (R^2 = 0.991) is higher than those of the Langmuir (R^2 = 0.979) and Temkin (R^2 = 0.919) models. Therefore, the Freundlich model is the most suitable isotherm model to accurately depict the adsorption system, revealing that the OG uptake occurred in a multiple-layer form on the heterogeneous PANi@DPC surface. In addition, the $1/n$ value is less than 1, which demonstrates that the OG dye adsorption on the PANi@DPC composite is favorable.[49]

3.2.3. Comparison of adsorption performance. The adsorption performance of PANi@DPC composite for OG removal was compared with that of other adsorbent materials. Table 3 depicts a comparative analysis of various adsorbents in terms of adsorption capacity, pH and optimal contact time. The PANi@DPC hybrid composite demonstrates a maximum OG dye uptake of 69.77 mg g^{-1}, which is comparable to or higher than those of most reported adsorbents (*e.g.*, PANi-modified

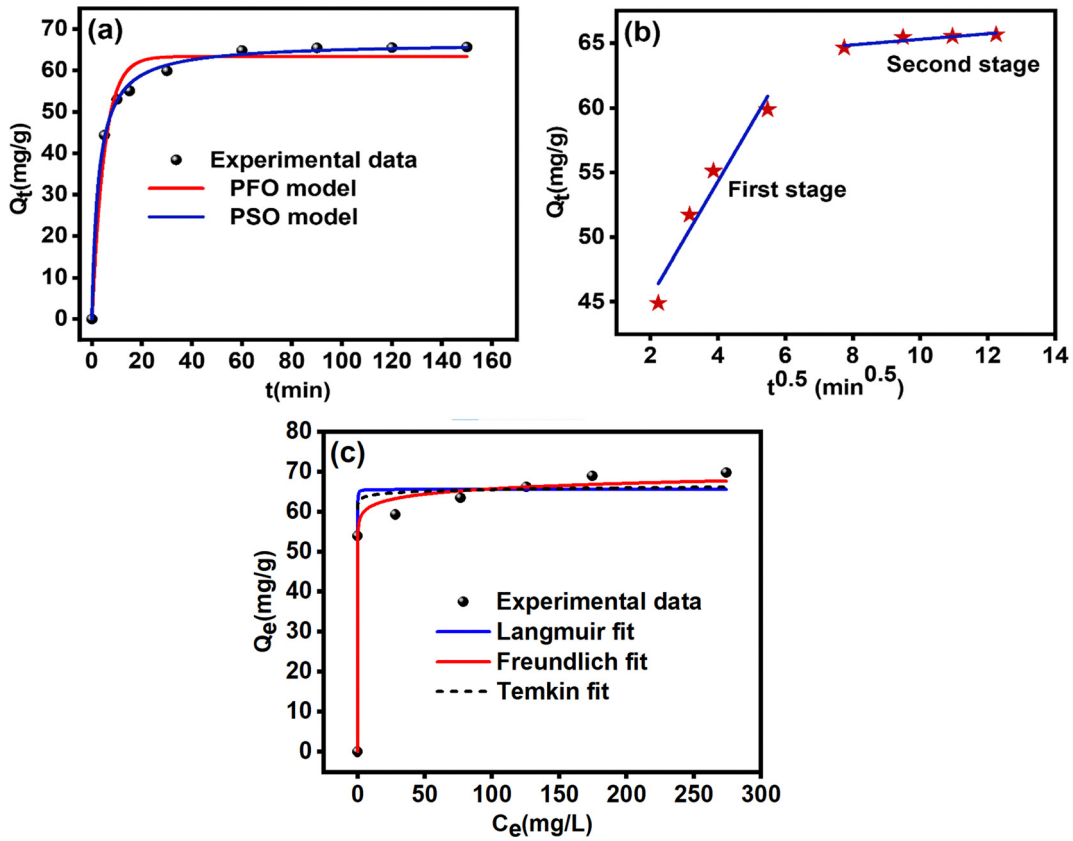

Fig. 6 (a) Nonlinear fitting plots of PFO and PSO equations, (b) multi-linear plots of the IPD model and (c) Langmuir, Freundlich and Temkin isotherm plots for OG adsorption onto the PANi@DPC composite.

Table 2 Kinetic and isotherm parameters for OG dye removal by the PANi@DPC hybrid composite

Kinetic models						
$Q_{e.exp}$ (mg g^{-1})	PFO model $Q_t = Q_{e.1}(1 - e^{(-k_1 t)})$			PSO model $Q_t = \frac{Q_{e.2}^2 k_2 t}{1 + Q_e k_2 t}$		
	k_1	$Q_{e.1}$	R^2	k_2	$Q_{e.2}$	R^2
65.65	0.205	63.36	0.975	0.005	66.71	0.997
IPD model: $Q_t = k_{1PD}t^{1/2} + C$						
First stage				Second stage		
k_{IPD1}	C_1	R^2		k_{IPD2}	C_2	R^2
4.469	36.413	0.944		0.215	63.13	0.816
Isotherm models						
$Q_{max.exp}$ (mg g^{-1})	Langmuir $Q_e = \frac{Q_{max} K_L C_e}{1 + K_L C_e}$			Freundlich $Q_e = K_F C_e^{1/n}$			Temkin $Q_e = \beta \ln K_T C_e$		
	Q_{max}	K_L	R^2	n_f	K_F	R^2	β	K_T	R^2
69.77	65.539	90.768	0.979	33.747	57.312	0.991	0.613	2.266	0.919

almond shells, PANi-modified walnut shells, bagasse fly ash, monoamine modified magnetic silica, monoamine modified magnetite free silica, modified nanoclay, cts(x)-*g*-PNVP and L-Arg-polypyrrole@g-C_3N_4 nanocomposite). Although Fe_3O_4/MIL-101(Cr) and crab shell powder exhibited higher maximum adsorption capacities compared to the PANi@DPC composite. However, these adsorbent materials operated in highly acidic conditions (pH 3.0), which brings additional wastewater

Table 3 Comparative table of the maximum adsorption capacity of the PANi@DPC composite with other adsorbents for OG dye removal

Adsorbents	Maximum adsorption capacity (mg g^{-1})	pH	Equilibrium time (min)	Ref.
PANi-modified almond shells	8.92	6	180	57
PANi-modified walnut shells	17.25	6	180	
Bagasse fly ash	18.79	4	240	58
Monoamine modified magnetic silica	61.33	3	60	59
Monoamine modified magnetite free silica	48.98	3	180	
Modified nanoclay	39.4	8	60	60
Fe_3O_4/MIL-101(Cr)	200	3	120	61
Crab shell powder	135.5	3	180	62
cts(x)-*g*-PNVP	63.7	3	180	63
L-Arg-polypyrrole@g-C_3N_4 nanocomposite	23.31	5.45	60	29
PANi@DPC composite	69.77	6.17	120	This study

treatment costs (*e.g.*, pH adjustment and potential corrosion of wastewater treatment facilities). In addition, the adsorption of OG dye onto crab shell powder required a relatively long time (180 min) to reach adsorption equilibrium. Therefore, the PANi@DPC composite has the potential to be a promising alternative for the treatment of OG dye-containing effluents.

3.3. RSM-BBD statistical analysis

In the current work, RSM-BBD was applied to develop a statistical model and explore how the independent variables (PANi@DPC dose, OG dye concentration, and pH) and their reciprocal interactions influenced the dependent variable (% OG decolorization). To predict the OG dye removal efficiency (Y (%)), the following polynomial model was developed using Design-Expert software:

$$\begin{aligned} Y\,(\%) &= 64.770 + 120.953 \cdot X_A - 0.697 \cdot X_B - 6.689 \cdot X_C \\ &\quad - 0.183 \cdot X_{A/B} - 1.415 \cdot X_{A/C} - 0.008 \cdot X_{B/C} \\ &\quad - 29.528 \cdot {X_A}^2 + 0.002 \cdot {X_B}^2 + 0.593 \cdot {X_C}^2 \end{aligned} \quad (5)$$

Based on the mathematical model, it is evident that X_A, X_C and ${X_A}^2$ terms exert a more pronounced impact on the OG dye removal performance. The PANi@DPC dose (X_A) proved to be the most predominant influencing parameter on the OG dye removal performance, with a positive effect (+120.953). The corresponding quadratic coefficient (${X_A}^2$) was found to be negative (−29.528), indicating that removal efficiency as a function of adsorbent dosage followed a concave curve.[64] Moreover, the solution pH (X_C) has a negative linear influence on the OG removal performance (−6.689). Finally, less significant interactions were observed between the tested parameters.

Analysis of variance (ANOVA) was utilized to evaluate the appropriateness of the as-developed RSM model (Table 4). The significance of the established RSM model and model terms (selected factors and their interactions) was verified based on *p*-values with a confidence level of 95%. Accordingly, the model terms with a *p*-value below 0.05 are statistically significant, whereas the other model terms are insignificant.[65] As a result, the actual data of the OG adsorption onto PANi@DPC composite are adequately described by the quadratic model with a lower *p*-value (0.0004). The as-developed RSM model presented a lack of fit that was statistically significant (<0.05); however, the correlation coefficient (R^2 = 0.9594) and the agreement between experimental and predicted values indicate that the model still provides a reliable description of the OG dye adsorption process. The adequate precision value is another criterion for determining the fitting accuracy of the RSM model, whose value must be higher than 4 for a good fit.[66] In the current study, the adequate precision value

Table 4 ANOVA and statistical parameters for OG adsorption onto the PANi@DPC hybrid composite

Source	Sum of squares	df	Mean square	*F*-Value	*p*-Value	
Model	14 831.77	9	1647.97	18.40	0.0004	Significant
X_A-PANi@DPC dose	6145.52	1	6145.52	68.62	<0.0001	
X_B-OG concentration	6696.14	1	6696.14	74.76	<0.0001	
X_C-pH	186.82	1	186.82	2.09	0.1919	
X_AX_B	175.30	1	175.30	1.96	0.2045	
X_AX_C	25.96	1	25.96	0.2898	0.6070	
X_BX_C	30.86	1	30.86	0.3445	0.5757	
${X_A}^2$	150.54	1	150.54	1.68	0.2359	
${X_B}^2$	1031.98	1	1031.98	11.52	0.0115	
${X_C}^2$	380.24	1	380.24	4.25	0.0783	
Residual	626.96	7	89.57			
Lack of fit	608.52	3	202.84	44.02	0.0016	
Pure error	18.43	4	4.61			
Cor total	15458.73	16				

Model statistics	R^2	Adjusted R^2	Adequate precision
	0.9594	0.9073	15.06

was found to be 15.06 (>4), confirming the RSM model's reliability. Besides, the model terms X_A, X_B and X_B^2 are statistically significant because of their low p-values (<0.05), while the other terms (X_C, X_{AB}, X_{AC}, X_{BC}, X_A^2 and X_C^2) are insignificant.

3D response surface plots can be used to assess the impact of individual factors and their reciprocal interactions on the OG dye decolorization performance. Fig. 7(a) shows 3D surface plot of the binary effect of PANi@DPC dosage and OG dye concentration.

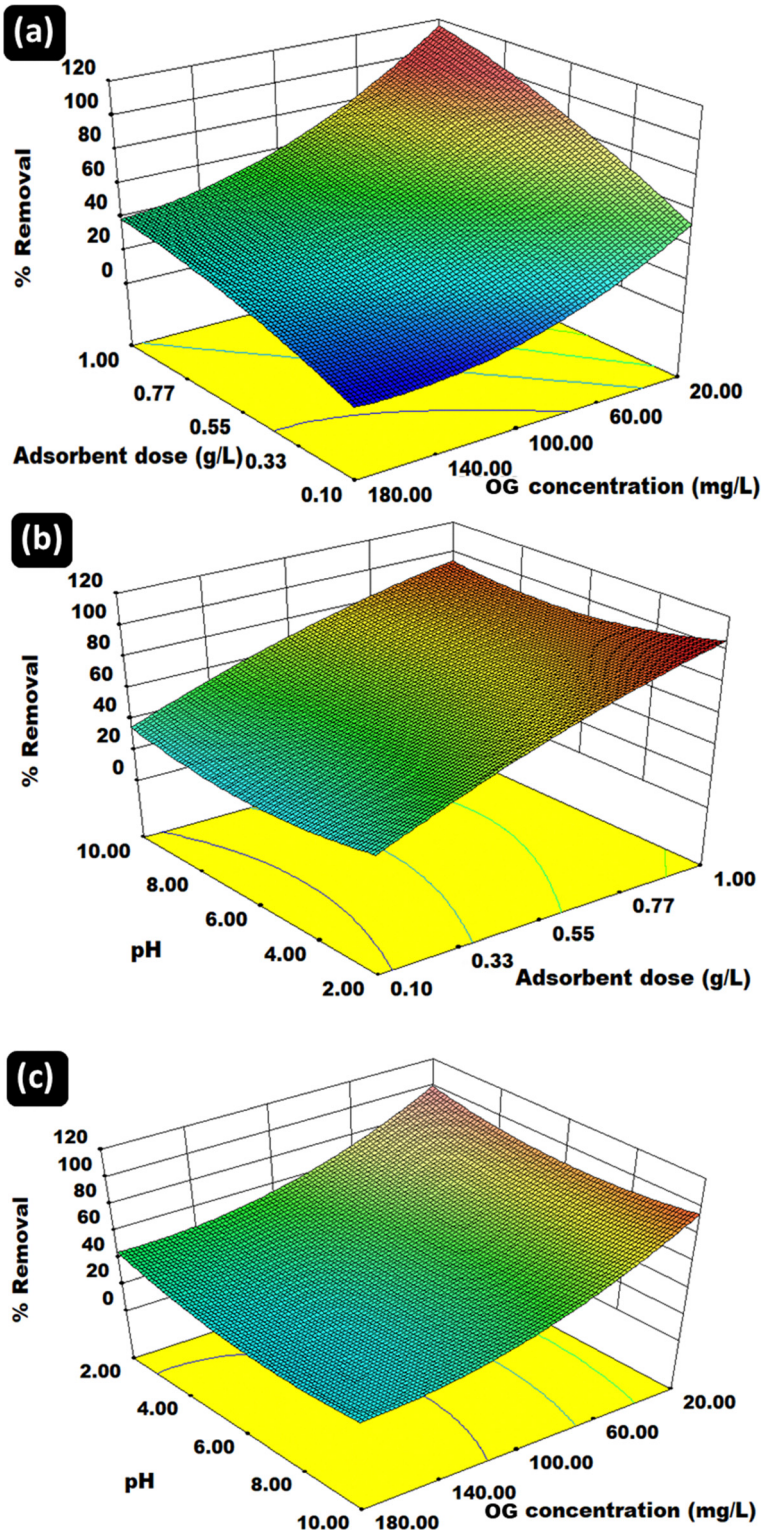

Fig. 7 3D surface graphs demonstrating the mutual effects between (a) PANi@DPC dose and OG concentration, (b) PANi@DPC dose and pH, and (c) OG concentration and pH on the OG removal efficiency.

As a result, the OG adsorption yield increased to reach a maximum of 99.62% with increasing the PANi@DPC dose from 0.1 to 1.0 g L^{-1} and decreasing the OG concentration from 180 to 20 mg L^{-1}. This is consistent with the fact that a high PANi@DPC dose offers more active sites for OG dye adsorption. Conversely, an increase in OG dye concentration might lead to the saturation of binding sites of the PANi@DPC composite and subsequently a decrease in OG removal efficiency. Fig. 7(b) shows that the solution pH has a negligible impact on the OG removal yield, allowing PANi@DPC composite to efficiently remove OG dye over a wide pH range in both acidic and alkaline environments. Finally, Fig. 7(c) clearly confirms the above observations, which again highlights the limited influence of pH on the OG adsorption in the studied pH range. Furthermore, the 3D surface plot underlines the negative effect of OG concentration due to the progressive saturation of PANi@DPC surface sites. Based on the RSM optimization, the optimum operating conditions for the maximum OG adsorption yield (99.54%) were determined to be pH 6.0, a PANi@DPC dose of 1.0 g L^{-1}, an OG concentration of 20 mg L^{-1}, a temperature of 25 °C, and an adsorption time of 120 min.

3.4. Physicochemical interpretation *via* advanced statistical physics

In the current study, experimental equilibrium data were analyzed using five advanced statistical physics models. The regression parameters are presented in Table S2. The appropriateness of the tested models to predict the OG adsorption onto PANi@DPC composite was assessed based on the R^2 and RMSE values. Thus, the model M2 exhibited outstanding correlation with the actual data, as indicated by high R^2 values (0.9998–0.9999) and low RMSE values (0.261–0.465). Thus, the model M2 demonstrated the highest predictive accuracy for the OG dye adsorption process at all studied temperatures. Consequently, the M3 model was selected to explain thermodynamic, energetic and stereographic aspects of the OG adsorption phenomenon on the PANi@DPC surface at a micro-level.

3.4.1. Statistical physics parameters. The stereographic and energetic features of the OG dye adsorption on the PANi@DPC composite can be evidenced using four main physicochemical parameters: n, N_M, saturation uptake capacity (Q_{sat}) and adsorption energies (E). These parameters were acquired from the best-fitting statistical physics model (M2). The stoichiometric coefficient n represents the average number of adsorbed OG molecules per binding site on the PANi@DPC surface (Fig. 8(a)). For the first type of active site, the values of n_1 consistently remain below one (0.132 at 25 °C, rising to 0.2919 at 45 °C), revealing that several OG molecules are adsorbed simultaneously on the receptor site through a multi-anchorage mechanism.[49] This indicates that each OG molecule interacts with multiple binding sites simultaneously,

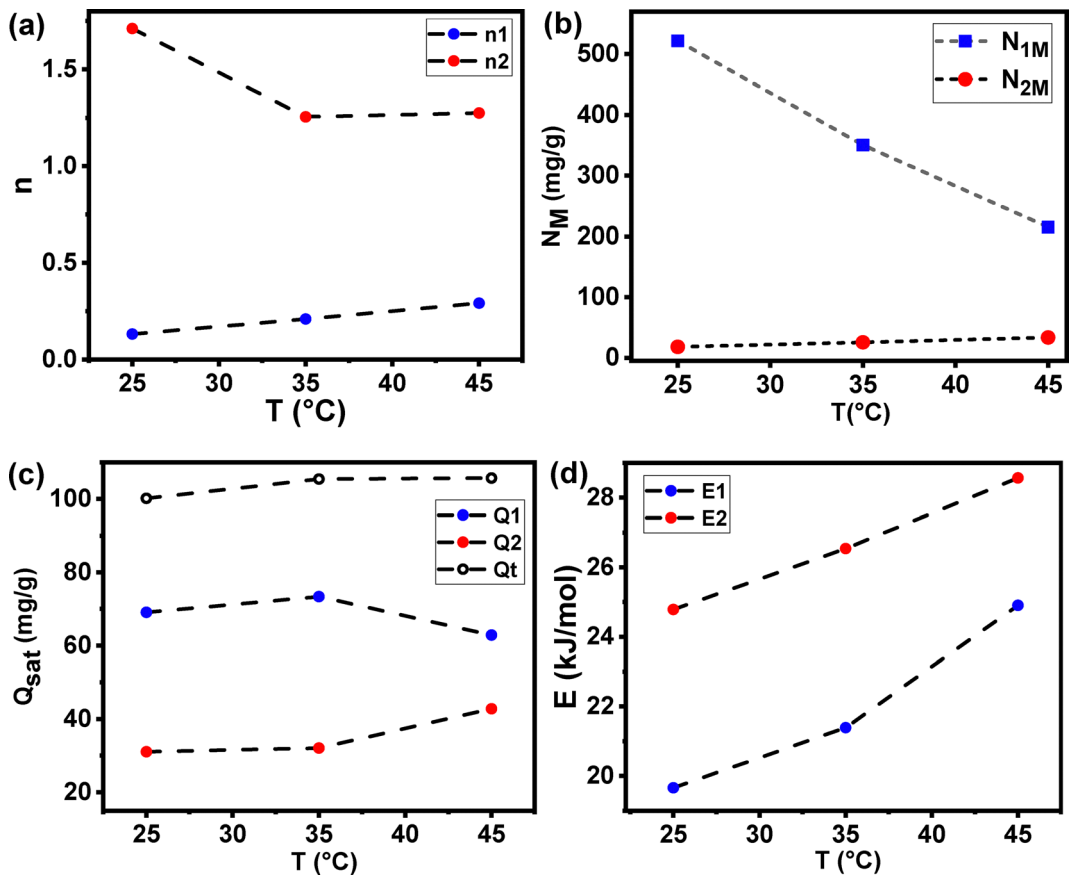

Fig. 8 Evolution of physicochemical parameters: (a) n, (b) N_M, (c) Q_{sat} and (d) E as a function of temperature for OG dye adsorption on the PANi@DPC hybrid composite.

which is likely attributed to its large molecular size and numerous functional moieties. The increment in n_1 with temperature suggests that thermal energy boosts the molecule's capacity to engage with fewer binding sites, possibly by overcoming steric hindrances.[67]

The n_2 values for the second type of binding sites surpass unity at all temperatures, starting from 1.711 at 25 °C and decreasing to 1.2751 at 45 °C. This suggests a mechanism of multi-molecular adsorption, indicating that several OG molecules can potentially interact with a single binding site of the second type through stacking or aggregation.[68] The decrease in n_2 as temperature increases may be due to the disruption of these molecular aggregates caused by increased thermal agitation. It is worth noting that $n_2 > n_1$ for all studied temperatures, indicating that the second type of active sites exhibits a greater adsorption affinity for OG molecules. This is possibly because of stronger interactions or a more favorable spatial arrangement for holding the OG molecules.

The density of receptor sites (N_M) offers insights into the ability of the PANi@DPC surface to adsorb OG molecules (Fig. 8(b)). At 25 °C, N_{1M} values are notably higher than N_{2M} values (521.764 compared to 18.152), indicating a greater abundance of the first type of binding sites on the PANi@DPC surface. However, N_{1M} decreases as temperature rises to 45 °C (216.351), while N_{2M} slightly increases (33.5693 at 45 °C). The inverse correlation between N_M and n values for both types of active sites can be attributed to steric effects. As the interaction of OG molecules with each site increases (n), the available space for additional binding sites decreases (N_M decreases). Q_{sat1} and Q_{sat2} were derived from n_1, n_2, N_{1M} and N_{2M} values (Fig. 8(c)). Interestingly, regardless of the opposing trends of n and N_M, both Q_{sat1} and Q_{sat2} increase with temperature. This suggests that the changes in binding site density have a greater influence on the adsorption capacity than the number of OG molecules per site. The total saturation uptake capacity ($Q_{sat.Tot}$) rises from 100.125 mg g^{-1} at 25 °C to 105.663 mg g^{-1} at 45 °C, confirming that the OG molecules exothermically adsorb on the PANi@DPC hybrid composite.[42]

The E_1 and E_2 values were calculated for both receptor site types and then plotted against temperature (Fig. 8(d)). Both E_1 and E_2 are positive and increase with temperature (E_1 = 19.657 to 24.9022 kJ mol^{-1}; E_2 = 24.785 to 28.9634 kJ mol^{-1} from 25 °C to 45 °C), confirming the endothermic nature of the OG adsorption process on the PANi@DPC composite. The nearly linear growth in adsorption energies with temperature suggests that higher temperatures promote the adsorption process, potentially by supplying the necessary energy to overcome adsorption barriers. In addition, E_2 values surpass E_1 values at all temperatures, indicating that the second type of adsorption sites interacts more strongly with OG molecules than the first type. This corresponds with the higher n_2 values observed in the stereographic analysis. The contrast in adsorption energies may be due to the chemical properties of the two types of binding sites. Given the composition of the PANi@DPC composite, it can be inferred that the first type of site (E_1) could be linked to the aromatic rings, potentially involving π–π interactions with the OG dye molecules.[42] The second type of adsorption sites (E_2) might be associated with the heteroatom-containing functional groups (amine and imine), potentially providing stronger hydrogen bonding for the OG molecules.

Throughout the temperature range, it is noteworthy that both E_1 and E_2 values remain below 40 kJ mol^{-1}. This observation implies that the OG adsorption onto the PANi@DPC composite occurs *via* physical interactions such as H-bonding and π–π stacking, rather than chemical bonding. The prevalence of physical adsorption mechanisms holds important implications for the potential reusability and regeneration of the PANi@DPC composite. This suggests that the desorption of OG should be achievable, which is a desirable attribute for practical applications in wastewater treatment.

3.4.2. Thermodynamic functions. To assess the spontaneity of OG dye adsorption on the PANi@DPC composite, the free enthalpy function $\left(\frac{G}{k_B T}\right)$ was calculated using the following equation.[49]

$$\frac{G}{k_B T} = \ln\left[\frac{\mu}{Z_{tr}}\right]\left(\frac{Q_{sat.1}}{1+\left[\frac{C_1}{C}\right]^{n_1}} + \frac{Q_{sat.2}}{1+\left[\frac{C_2}{C}\right]^{n_2}}\right) \quad (6)$$

In eqn (6), k_B, μ and Z_{tr} represent Boltzmann's constant, chemical potential and translational partition function, respectively.

Fig. 9(a) shows the evolution of free enthalpy as a function of OG concentration at different temperatures. All free enthalpy values are negative, suggesting that the OG adsorption process is spontaneous. Besides, the absolute magnitude of free enthalpy increases with temperature, revealing that the OG dye adsorption process is more suitable at higher temperatures.[42]

The entropy function $\left(\frac{S}{k_B}\right)$ is of prime importance for a deeper characterization of the solid–liquid interface during the adsorption phenomenon. This thermodynamic function can be determined using statistical physics formalism as follows:[49]

$$\frac{S}{k_B} = \frac{-Q_{sat.1}\left[\frac{C}{C_1}\right]^{n_1}\ln\left[\frac{C}{C_1}\right] + Q_{sat.2}\left[\frac{C}{C_2}\right]^{n_2}\ln\left[\frac{C}{C_2}\right] + \left[\frac{C}{C_1}\right]^{n_1}\left[\frac{C}{C_2}\right]^{n_2}\left(Q_{sat.1}\ln\left[\frac{C}{C_1}\right] + Q_{sat.2}\ln\left[\frac{C}{C_2}\right]\right)}{\left(1+\left[\frac{C}{C_1}\right]^{n_1}\right)\left(1+\left[\frac{C}{C_2}\right]^{n_2}\right) + \ln\left(\left(1+\left[\frac{C}{C_1}\right]^{n_1}\right)^{N_{1M}}\left(1+\left[\frac{C}{C_2}\right]^{n_2}\right)^{N_{2M}}\right)} \quad (7)$$

Fig. 9(b) illustrates the variations of the entropy function *versus* dye concentration for OG adsorption on the PANi@DPC hybrid composite at various temperatures. It can be seen that the entropy function displays an analogous tendency for all

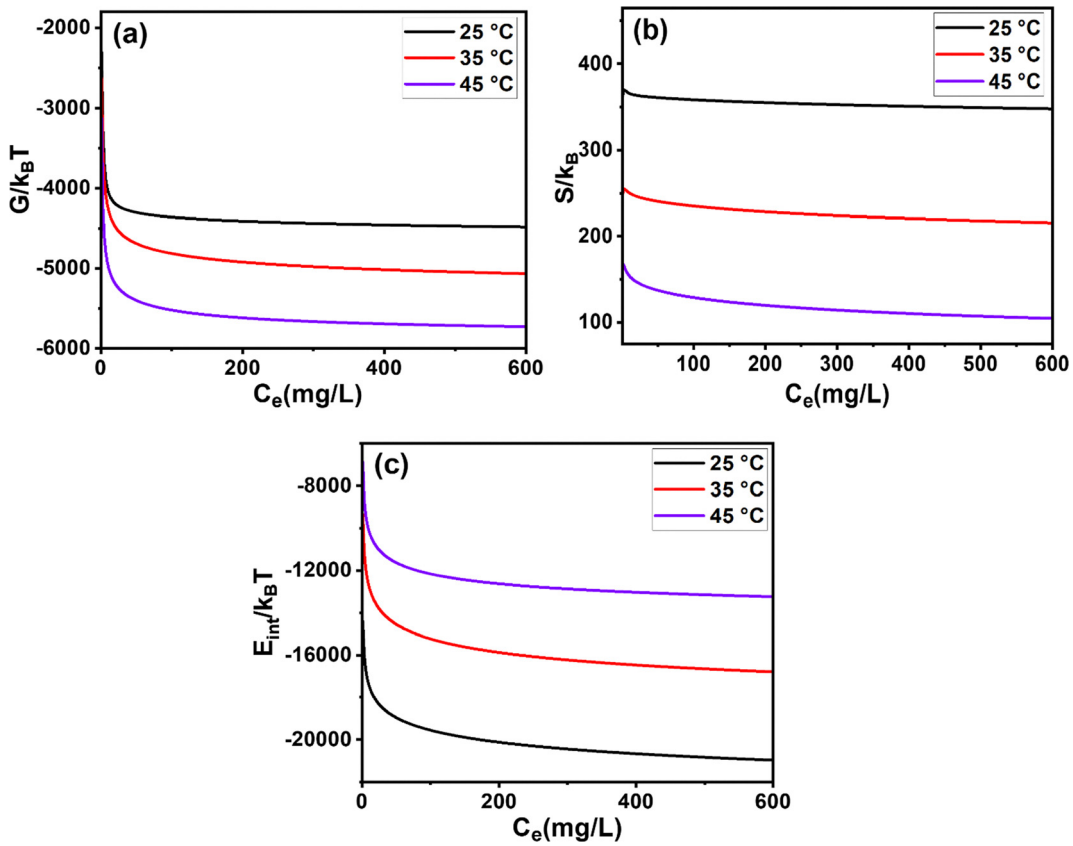

Fig. 9 Representations of (a) free enthalpy, (b) entropy and (c) internal energy functions for OG dye adsorption on the PANi@DPC composite.

temperatures. As the equilibrium OG dye concentration increases, the entropy at the solid–liquid interface for the OG dye adsorption process increases gradually. At low concentrations, the entropy is fairly important. This affirms that the adsorbate molecules have a higher possibility of selecting a binding site on the PANi@DPC composite, leading to a high degree of disorder at the liquid–adsorbent interface. However, as the adsorbate concentration increases and the PANi@DPC surface tends to saturation, OG molecules have insufficient possibilities to find a free active site. Thus, the entropy function (degree of disorder) decreased.[49]

The last thermodynamic function is the internal energy $\left(\frac{E_{int}}{k_B T}\right)$, which represents the adsorption energy arising from the dye–adsorbent interactions during the adsorption process. The formulation of internal energy function is given below:[42]

$$\frac{E_{int}}{k_B T} = \frac{-N_{1M}\left[\frac{C}{C_1}\right]^{n_1}\left(n_1 \ln\left[\frac{C}{C_1}\right] - \mu\right) + N_{2M}\left[\frac{C}{C_2}\right]^{n_2}\left(n_2 \ln\left[\frac{C}{C_2}\right] - \mu\right) + \left[\frac{C}{C_1}\right]^{n_1}\left[\frac{C}{C_2}\right]^{n_2}\left(N_{1M}\left(n_1 \ln\left[\frac{C}{C_1}\right] - \mu\right) + N_{2M}\left(n_2 \ln\left[\frac{C}{C_2}\right] - \mu\right)\right)}{\left(1 + \left[\frac{C}{C_1}\right]^{n_1}\right)\left(1 + \left[\frac{C}{C_2}\right]^{n_2}\right)} \quad (8)$$

The evolution of $\left(\frac{E_{int}}{k_B T}\right)$ against OG dye concentration is depicted in Fig. 9(c). As a result, it is evident that the E_{int} values are negative, suggesting that the OG adsorption system releases energy to the outside.[49] Hence, the PANi@DPC surface possessed high affinity to adsorb OG dye molecules. Additionally, E_{int} decreases significantly at lower OG dye concentrations, suggesting that the OG dye molecules favorably adsorb on the high-energy binding sites on the PANi@DPC composite. As the OG concentration increases, the availability of the adsorption sites diminishes, forcing the OG dye molecules to adsorb on the low-energy active sites, which leads to a slight reduction in E_{int} values.[49] Furthermore, it is shown that the module of E_{int} for the OG adsorption process decreases with rising temperature. This thermodynamic behavior might be ascribed to the reduction in thermal collision.[69]

3.5. Binding mechanism

To illuminate the OG adsorption mechanism, the OG dye-loaded PANi@DPC composite was analyzed using FTIR spectroscopy. From Fig. 10(a), the absorption bands associated with the quinonid (1598 cm^{-1}), benzenoid (1446 cm^{-1}) and –NH groups (3439 cm^{-1}) are slightly red-shifted and weakened.

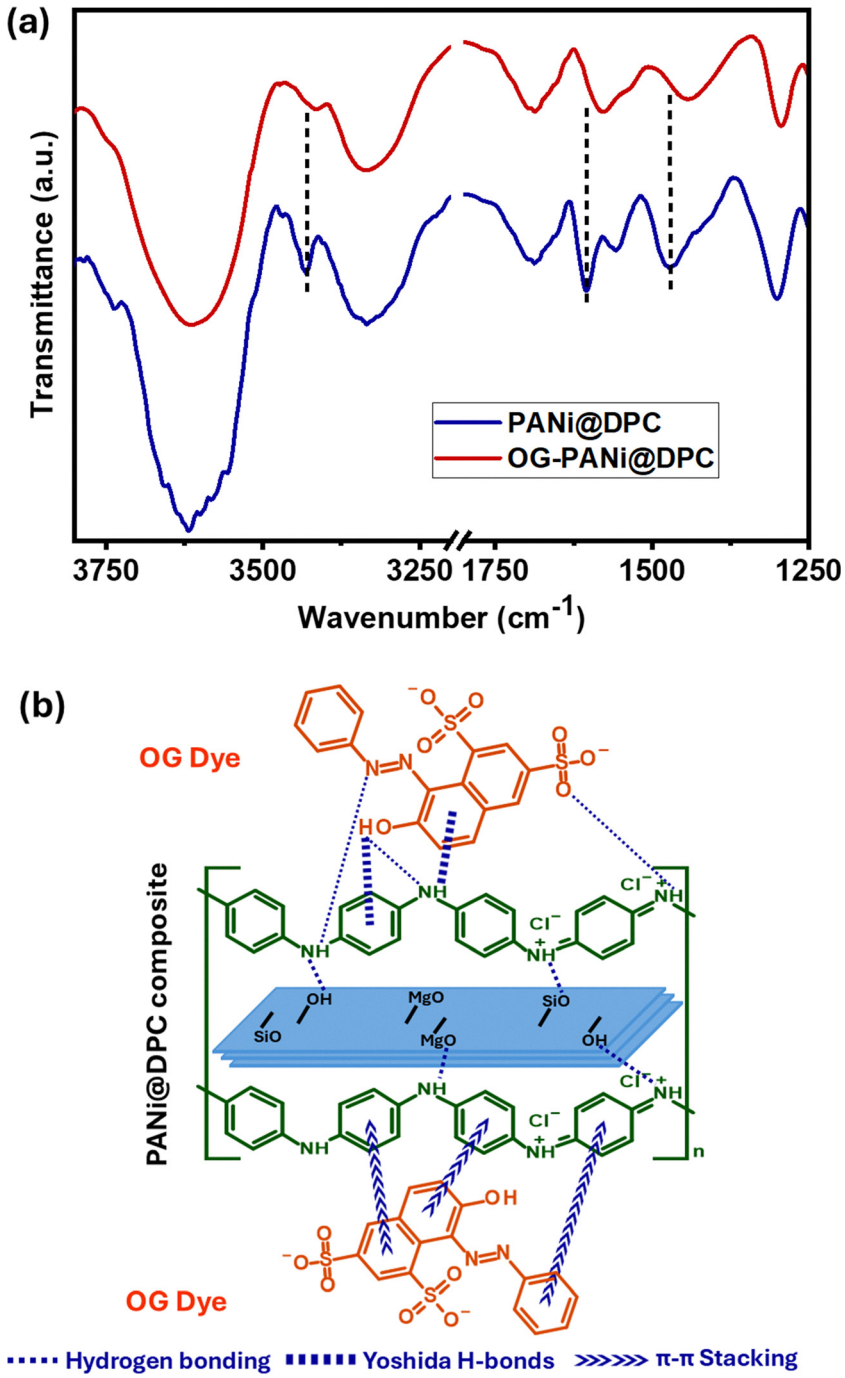

Fig. 10 (a) FTIR spectrum of PANi@DPC composite after OG dye adsorption, and (b) schematic representation of the proposed OG dye binding mechanism.

These spectral alterations signify the involvement of the nitrogen-containing groups and aromatic rings of the PANi@DPC composite in the OG dye binding mechanism.[70] The spectral peak corresponding to the N–H vibrations is redshifted by 23 cm^{-1} and broadened after OG dye adsorption, confirming the formation of H-bonds.[71] H-bonds can be formed between the H-donor of amine/imine groups of PANi@DPC and oxygen (N–H···O) or nitrogen (N–H···N) atoms of the OG dye molecule. Another type of hydrogen bond could be possible between the H-donor of the hydroxyl group of OG dye and nitrogen atoms of PANi@DPC (O–H···N). The benzene rings of OG dye can act as H-acceptors in the Yoshida hydrogen bonding with N–H of the PANi@DPC composite.[72] Structurally, both PANi@DPC composite and OG dye molecule contain benzene rings, which means that π–π stacking should be considered in the OG binding mechanism. This suggestion is confirmed by the red shift of the absorption bands associated with aromatic rings of PANi@DPC composite.[70] It is worth

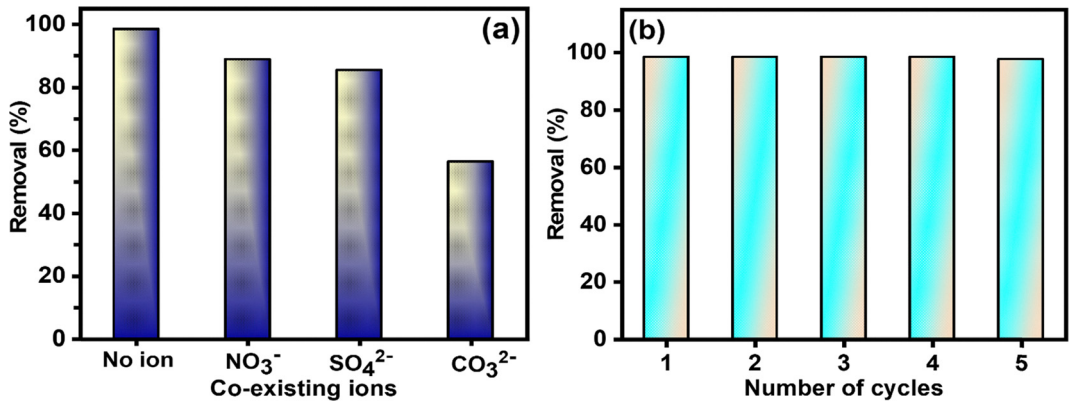

Fig. 11 (a) Influence of interfering ions on the OG dye decolorization by the PANi@DPC composite (pH = 6.17; equilibrium time = 2 h; adsorbent dose = 0.375 g L^{-1}; 25 mg L^{-1} OG concentration; T = 298 K) and (b) OG dye removal yield for 5 times reuse of the PANi@DPC composite.

noting that π–π stacks and H-bonds act as the primary non-electrostatic driving forces behind OG dye adsorption, especially at pH > PZC, which decreased slightly in the pH range of 2.6–9.8. Likewise, the interplay of H-bonds and π–π stacking might generate a synergistic effect on the OG adsorption on the PANi@DPC surface.[73] A schematic representation of the proposed OG dye binding mechanism is depicted in Fig. 10(b).

3.6. Influence of interfering ions and adsorbent recycling

Besides synthetic dyes, wastewater is also contaminated by other organic and mineral contaminants. The textile effluents often contain inorganic salts, such as nitrate (NO_3^-), sulfate (SO_4^{2-}), and carbonate (CO_3^{2-}). For this reason, the influence of co-existing inorganic ions on the OG adsorption by the PANi@DPC composite must be assessed. From Fig. 11(a), the OG decolorization yield was slightly reduced from 98.46% to 88.77% and 85.41% in the presence of NO_3^- and SO_4^{2-} ions, respectively. This adsorption behavior further confirmed that the OG dye adsorption onto PANi@DPC surface is predominantly governed by non-electrostatic interactions.[74] However, CO_3^{2-} ions have a meaningful antagonistic effect on the OG removal efficiency. A possible explanation for this adsorption behavior is the affinity of the PANi@DPC surface for CO_3^{2-} ions, which compete with OG molecules and thereby inhibit OG adsorption. Besides, the addition of Na_2CO_3, an alkaline salt, increases the solution pH (hydrolysis reaction) and subsequently reduces the adsorption performance of PANi@DPC surface toward OG anionic dye.[75]

In addition to good removal effectiveness, recycling ability is also considered a key advantage, which makes the adsorbent a promising choice for wastewater treatment. The reusability of PANi@DPC composite for OG dye removal from water was investigated over 5 cycles. Based on the reversible acid/base doping/de-doping in PANi, the exhausted PANi@DPC composite was effortlessly regenerated using NaOH solution.[49] Fig. 11(b) indicates that the reusability of the PANi@DPC composite remains almost the same (~98.50%) for the first 4 regeneration cycles. Then, the OG removal efficiency slightly decreases to 97.60% during the 5th reuse cycle due to the partial desorption of the OG molecules. In summary, the PANi@DPC composite can be easily reused several times with excellent OG dye removal performance.

4. Conclusions

The PANi@DPC hybrid composite was successfully elaborated and applied as a potential binder material for effective decolorization of OG dye from an aqueous medium. The as-developed PANi@DPC composite exhibited high removal capacity for OG dye over a large pH range (2.6–8.4). The maximum uptake capacity of the PANi@DPC composite for OG dye was 69.77 mg g^{-1} at pH 6.17, which is competitive with that of other adsorbents. The actual data conforms to the PSO (R^2 = 0.997) and Freundlich (R^2 = 0.991) isotherm models. The IPD model indicates that the OG dye mass transfer process occurs through both film diffusion and pore diffusion. RSM investigation revealed that the positive linear effect of PANi@DPC dose and its negative quadratic effect are the most influential factors for OG dye adsorption. Additionally, RSM optimization findings have proven that the maximum predicted OG dye adsorption performance (99.54%) was achieved under optimal operating conditions (pH 6.0, PANi@DPC dosage of 1.0 g L^{-1}, OG concentration of 20 mg L^{-1}, temperature of 25° and adsorption time of 120 min). Advanced statistical physics modeling revealed that the OG dye adsorption occurred spontaneously $\left(\frac{G}{k_B T} < 0\right)$ *via* multi-docking ($n_1 < 1$) and multi-molecular ($n_2 > 1$) mechanisms. In addition, the OG adsorption is mainly an endothermic physisorption type. The OG binding mechanism is mainly assigned to π–π interactions, H-bonding and Yoshida H-bonds. The regeneration of the PANi@DPC composite has demonstrated outstanding OG dye removal performance (97.60%) after five reuse cycles. Overall, the PANi@DPC composite demonstrates significant potential for sustainable applications, and the findings of the present study are undoubtedly promising. Although this study focused on synthetic OG dye solutions under controlled conditions,

evaluating the economic feasibility of the PANi@DPC hybrid composite for real wastewater treatment.

Conflicts of interest

The authors declare no conflicts of interest.

Data availability

Data for this article are available from the corresponding author.

Supplementary information is available. See DOI: https://doi.org/10.1039/d5ma00660k.

References

1 M. D. Khan, A. Singh, M. Z. Khan, S. Tabraiz and J. Sheikh, *J. Water Process Eng.*, 2023, **53**, 103579.
2 J. Lin, W. Ye, M. Xie, D. H. Seo, J. Luo, Y. Wan and B. Van der Bruggen, *Nat. Rev. Earth Environ.*, 2023, **4**(11), 785–803.
3 Y. Shi, Z. Yang, L. Xing, X. Zhang, X. Li and D. Zhang, *World J. Microbiol. Biotechnol.*, 2021, **37**(8), 1–18.
4 U. M. Lekhak, *Current Developments in Bioengineering and Biotechnology: Advances in Eco-friendly and Sustainable Technologies for the Treatment of Textile Wastewater*, 2023, pp. 45–67.
5 S. H. Hashemi and M. Kaykhaii, *Emerging Freshwater Pollutants: Analysis, Fate and Regulations*, 2022, pp. 267–287.
6 B. Monisha, R. Sridharan, P. S. Kumar, G. Rangasamy, V. G. Krishnaswamy and S. Subhashree, *Chemosphere*, 2023, **313**, 137614.
7 S. S. Emmanuel, A. A. Adesibikan, E. A. Opatola and C. O. Olawoyin, *Appl. Organomet. Chem.*, 2023, **37**, e7108.
8 D. Ma, Q. Xue, Y. Liu, F. Liang, W. Li, T. Liu, C. Zhuang, Z. Zhao and S. Li, *J. Mater. Sci. Technol.*, 2026, **243**, 265–274.
9 S. Li, C. You, K. Rong, C. Zhuang, X. Chen and B. Zhang, *Adv. Powder Mater.*, 2024, **3**, 100183.
10 C. Valli Nachiyar, A. D. Rakshi, S. Sandhya, N. Britlin Deva Jebasta and J. Nellore, *Case Stud. Chem. Environ. Eng.*, 2023, **7**, 100339.
11 M. S. S. Abujazar, S. U. Karaağaç, S. S. Abu Amr, M. Y. D. Alazaiza and M. J. Bashir, *J. Cleaner Prod.*, 2022, **345**, 131133.
12 P. Moradihamedani, *Polym. Bull.*, 2022, **79**, 2603–2631.
13 M. Cai, Y. Liu, K. Dong, X. Chen and S. Li, *Chin. J. Catal.*, 2023, **52**, 239–251.
14 C. Wang, K. Rong, Y. Liu, F. Yang and S. Li, *Sci. China Mater.*, 2024, **67**, 562–572.
15 J. Zhang, G. Yu, C. Yang, W. Zhao, Z. Duan, H. Liu and S. Li, *SusMat*, 2025, **5**, e70002.
16 J. Zhang, G. Yu, C. Yang and S. Li, *Curr. Opin. Chem. Eng.*, 2024, **45**, 101040.
17 D. Feng, X. Li, Y. Liu, X. Chen and S. Li, *Renewables*, 2023, **1**, 485–513.
18 M. Saeed, M. Muneer, A. ul Haq and N. Akram, *Environ. Sci. Pollut. Res.*, 2021, **29**(1), 293–311.
19 L. García, J. C. Leyva-Díaz, E. Díaz and S. Ordóñez, *Sci. Total Environ.*, 2021, **780**, 146554.
20 R. Agarwala and L. Mulky, *ChemBioEng Rev.*, 2023, **10**, 326–335.
21 B. Saha, A. Debnath and B. Saha, *J. Indian Chem. Soc.*, 2022, **99**, 100635.
22 G. G. Hacıosmanoğlu, C. Mejías, J. Martín, J. L. Santos, I. Aparicio and E. Alonso, *J. Environ. Manage.*, 2022, **317**, 115397.
23 D. Ewis, M. M. Ba-Abbad, A. Benamor and M. H. El-Naas, *Appl. Clay Sci.*, 2022, **229**, 106686.
24 P. Gao, D. Chen, W. Chen, J. Sun, G. Wang and L. Zhou, *Int. J. Biol. Macromol.*, 2021, **191**, 1240–1248.
25 M. Laabd, N. Aarab, H. Chafai, M. Bazzaoui, M. Elamine, R. Lakhmiri and A. Albourine, *Fibers Polym.*, 2017, **18**, 1064–1072.
26 J. Ding, W. Zhang, X. Dai, J. Yao and G. Gao, *J. Environ. Chem. Eng.*, 2022, **10**, 108926.
27 K. Jahan, S. Tyeb, N. Kumar and V. Verma, *J. Polym. Environ.*, 2021, **29**, 1257–1270.
28 A. Essekri, M. Laabd, A. Fatni, A. Ait Addi, R. Lakhmiri and A. Albourine, *Chem. Eng. Res. Des.*, 2023, **190**, 143–156.
29 F. Z. Mahir, H. Zouggari, A. Imgharn, A. A. Addi, K. A. El Bacha, A. M. Diez, M. Á. Sanromán, M. Laabd, A. Hsini, N. Aarab, L. Bazzi, R. Lakhmiri and A. Albourine, *Inorg. Chem. Commun.*, 2025, **172**, 113656.
30 B. Saha, G. Shil, A. Debnath and B. Saha, *J. Indian Chem. Soc.*, 2024, **101**, 101407.
31 M. A. Abdel-Rahman, S. E. D. Hassan, M. N. El-Din, M. S. Azab, E. F. El-Belely, H. M. A. Alrefaey and T. Elsakhawy, *SN Appl. Sci.*, 2020, **2**, 1–14.
32 M. F. P. da Costa, R. D. S. Araújo, A. R. Silva, L. Pereira and G. M. M. Silva, *Appl. Sci.*, 2025, **15**, 2310.
33 J. D. Nerona, N. C. M. Abella, G. A. G. C. Jundam and R. P. Gumaling, *J. Water Process Eng.*, 2024, **58**, 104851.
34 S. Kumari, J. Chowdhry, P. Sharma, S. Agarwal and M. Chandra Garg, *Chemosphere*, 2023, **344**, 140262.
35 A. Essekri, M. A. Haki, M. Laabd, A. A. Addi, R. Lakhmiri and A. Albourine, *Chem. Eng. Res. Des.*, 2023, **195**, 390–403.
36 M. Mobarak, E. A. Mohamed, A. Q. Selim, F. M. Mohamed, L. Sellaoui, A. Bonilla-Petriciolet and M. K. Seliem, *J. Mol. Liq.*, 2019, **285**, 678–687.
37 Y. Luo, J. Luo, Y. Hua, J. Yao, S. M. Chen and X. Liu, *Dalton Trans.*, 2018, **47**, 16855–16861.
38 J. Chisholm, *Ann. Occup. Hyg.*, 2005, **49**, 351–358.
39 X. Hou, Q. Cheng, J. Wang, Q. Wu and W. Zhang, *RSC Adv.*, 2021, **11**, 24416–24423.
40 J. M. Gregg, D. L. Bish, S. E. Kaczmarek and H. G. Machel, *Sedimentology*, 2015, **62**, 1749–1769.
41 M. A. Sayed and H. A. Nasr-El-Din, Proceedings – SPE International Symposium on Formation Damage Control, 2012, vol. 2, pp. 866–885.
42 A. Imgharn, L. Anchoum, A. Hsini, Y. Naciri, M. Laabd, M. Mobarak, N. Aarab, A. Bouziani, S. Szunerits,

R. Boukherroub, R. Lakhmiri and A. Albourine, *Chemosphere*, 2022, **295**, 133786.
43 J. J. Xie, T. Chen, B. Xing, H. Liu, Q. Xie, H. Li and Y. Wu, *Appl. Clay Sci.*, 2016, **119**, 42–48.
44 V. N. S. Campos, J. D. J. P. Santos, R. J. P. Araújo, P. H. S. Lopes, M. A. S. Garcia, A. Rojas, M. M. Teixeira, C. W. B. Bezerra and A. C. S. Alcântara, *Minerals*, 2024, **14**, 792.
45 V. C. Silva, M. E. B. Araújo, A. M. Rodrigues, J. M. Cartaxo, R. R. Menezes and G. A. Neves, *Sustainability*, 2021, **13**, 3954.
46 M. A. Hassaan and A. El Nemr, *Mar. Pollut. Bull.*, 2021, **173**, 113070.
47 S. Kadír, M. Eren and E. Atabey, *Clays Clay Miner.*, 2010, **58**, 205–219.
48 H. Pálková, J. Madejová, M. Zimowska and E. M. Serwicka, *Microporous Mesoporous Mater.*, 2010, **127**, 237–244.
49 M. Laabd, A. Imgharn, A. Hsini, Y. Naciri, M. Mobarak, S. Szunerits, R. Boukherroub and A. Albourine, *J. Hazard. Mater.*, 2022, **422**, 126857.
50 N. C. Nepomuceno, A. A. A. Seixas, E. S. Medeiros and T. J. A. Mélo, *J. Solid State Chem.*, 2021, **302**, 122372.
51 M. Sguillar, R. Lakhmiri, I. Eladnani, N. Ait Oukharaz, H. El Fargani, M. Laabd, A. Albourine, M. Safi and O. Cherkaoui, *Chem. Phys. Lett.*, 2024, **843**, 141234.
52 A. M. Elgamal, N. A. Abd El-Ghany and G. R. Saad, *Int. J. Biol. Macromol.*, 2023, **227**, 27–44.
53 X. Huang, H. Zhao, X. Hu, F. Liu, L. Wang, X. Zhao, P. Gao and P. Ji, *J. Hazard. Mater.*, 2020, **392**, 122461.
54 M. Laabd, Y. Brahmi, B. El Ibrahimi, A. Hsini, E. Toufik, Y. Abdellaoui, H. Abou Oualid, M. El Ouardi and A. Albourine, *J. Mol. Liq.*, 2021, **338**, 116705.
55 A. Essekri, M. Laabd and A. Albourine, *Colloids Surf., A*, 2024, **687**, 133401.
56 A. Deb, A. Debnath and B. Saha, *J. Dispersion Sci. Technol.*, 2021, **42**, 1579–1592.
57 A. Imgharn, H. ighnih, A. Hsini, Y. Naciri, M. Laabd, H. Kabli, M. Elamine, R. Lakhmiri, B. Souhail and A. Albourine, *Chem. Phys. Lett.*, 2021, **778**, 138811.
58 I. D. Mall, V. C. Srivastava and N. K. Agarwal, *Dyes Pigm.*, 2006, **69**, 210–223.
59 A. A. Atia, A. M. Donia and W. A. Al-Amrani, *Chem. Eng. J.*, 2009, **150**, 55–62.
60 M. A. Salam, S. A. Kosa and A. A. Al-Beladi, *J. Mol. Liq.*, 2017, **241**, 469–477.
61 T. Wang, P. Zhao, N. Lu, H. Chen, C. Zhang and X. Hou, *Chem. Eng. J.*, 2016, **295**, 403–413.
62 A. Laghzal, M. Hmamou, B. Boudinar, N. Nouj, H. Ighnih, F. Salmoun, E. M. Azzirgue and Y. Tligui, *Desalin. Water Treat.*, 2024, **320**, 100738.
63 Z. A. Sutirman, M. M. Sanagi, K. J. Abd Karim, A. Abu Naim and W. A. Wan Ibrahim, *Int. J. Biol. Macromol.*, 2019, **133**, 1260–1267.
64 R. Hazime, Q. H. Nguyen, C. Ferronato, T. K. X. Huynh, F. Jaber and J. M. Chovelon, *Appl. Catal., B*, 2013, **132–133**, 519–526.
65 M. H. Dehghani, K. Yetilmezsoy, M. Salari, Z. Heidarinejad, M. Yousefi and M. Sillanpää, *J. Mol. Liq.*, 2020, **299**, 112154.
66 B. Kumari, R. K. Tiwary and M. Yadav, *Mater. Chem. Phys.*, 2022, **290**, 126457.
67 L. Sellaoui, F. Dhaouadi, H. E. Reynel-Avila, D. I. Mendoza-Castillo, A. Bonilla-Petriciolet, R. Trejo-Valencia, S. Taamalli, F. Louis, A. El Bakali and Z. Chen, *Environ. Sci. Pollut. Res.*, 2021, **28**, 67248–67255.
68 M. Ben Manaa, N. Issaoui, N. Bouaziz and A. Ben Lamine, *J. Mater. Res. Technol.*, 2020, **9**, 1175–1188.
69 X. Yang, J. Wang, A. M. El-Sherbeeny, A. A. AlHammadi, W. H. Park and M. R. Abukhadra, *Chem. Eng. J.*, 2022, **431**, 134312.
70 J. Yang, J. Wang, X. Zhang, M. Chen, B. Tian, N. Wang, X. Huang and H. Hao, *Microporous Mesoporous Mater.*, 2022, **330**, 111624.
71 I. Ahmed, Z. Hasan, G. Lee, H. J. Lee and S. H. Jhung, *Chem. Eng. J.*, 2022, **430**, 132596.
72 I. A. Mohammed, A. H. Jawad, A. S. Abdulhameed and M. S. Mastuli, *Int. J. Biol. Macromol.*, 2020, **161**, 503–513.
73 Q. Lian, F. Islam, Z. U. Ahmad, X. Lei, D. Depan, M. Zappi, D. D. Gang, W. Holmes and H. Yan, *Chemosphere*, 2021, **280**, 130730.
74 V. L. Dang, T. T. Kieu, T. T. T. Nguyen, T. T. T. Truong, D. T. Hoang, T. L. C. Vu, T. M. T. Nguyen, T. S. Le, T. H. Y. Doan and T. D. Pham, *J. Mol. Struct.*, 2024, **1304**, 137619.
75 A. Dzieniszewska, J. Kyzioł-Komosińska and M. Pająk, *Desalin. Water Treat.*, 2020, **177**, 209–226.